

Chapter 5

Special feature synthesis for continuum edge spectral analysis

5.1 Series limit spectral modelling background

A complete spectrum for series limit wavelengths through to the continuum can now be generated as a function of basic plasma parameters. This synthetic spectrum is referred to as a ‘spectral feature’. To generate such a spectral feature it is necessary to bring together the population, line profile, opacity and continuity work presented thus far, the individual components of this feature being referred to as ‘feature primitives’. This is analogous to the collisional-radiative block primitives and blocks of chapter 4. This chapter outlines the method of high series spectral feature generation and demonstrates the use of a code tailored for JET divertor conditions.

ADAS contains various diagnostic codes that perform a maximum likelihood fit of a spectral feature to observational data. ADAS 602 fits gaussian profiles to an observed spectrum and was used in the line identification work mentioned in section 2.9 and Brooks et al. (1999), and in the doppler shift diagnostic work of Spadaro et al. (2000) which led to the first observations of siphon flows in the solar atmosphere. ADAS 603 fits Zeeman spectral features to an observed spectrum thus diagnosing parameters such as the plasma magnetic field. See Summers (2001) for a description of both of these codes. Given the worth of such fitting codes as plasma diagnostics, the series

limit feature work forms a natural addition to the ADAS suite of codes.

Consider the following expression for the optically thick emergent flux from a plasma of length of line of sight b , with no incident background radiation field:

$$I(\lambda) = \int_0^b \varepsilon(\lambda, \underline{r}) \Theta(\lambda) dl \quad (5.1)$$

The analytically continuous emission coefficient and escape probability expressions from chapter 3 are used. For applications such as those we are considering in this chapter it is also necessary to include other contributions to the emission coefficient such as those from other hydrogen continua, hydrogen bremsstrahlung emission and emission from plasma impurities. Section 5.2 deals in turn with all the contributions to equation (5.1). Section 5.3 describes a code that is being developed as a diagnostic tool for use in the divertor region of JET, with section 5.3.3 giving two example fits to observations with a corresponding diagnosis of plasma parameters.

5.2 General components of the series limit feature

5.2.1 Atomic populations

Since it is mainly high series hydrogen-like systems that are being considered at this stage, the high n-shell module of the population code described in chapter 4 is an appropriate means of evaluating the population distributions. The code evaluates b-factors for the populations up to arbitrary high n-shells for defined plasma parameters. A sample output datafile is shown in figure 5.1. The B(ACTUAL) column contains the b-factors for the populations. This is split up into various contributing parts, namely that from the ground state (metastable contributions can also be included in an extension of the code) in the F1 column, and the contribution from free-electron recombination in the F2 column. These contributions are then recombined independently to give the b-factor value B(CHECK), as a check to ensure that the separation procedure worked correctly without cancellation error.

The procedure is used in the spectral feature creation is as follows: the code is run for the required plasma parameters and a datafile as in figure 5.1 produced. The b-factor

values are then read from this file by the spectral feature code. Saha-Boltzmann populations are then modified by these b-values to give the resultant populations. Thus each different density and temperature parameter set requires a separate run of the population code. Although this increases the run-time for the feature generation, it is not a major issue for a final fitting code. A future ADAS fitting code will use a pre-calculated set of synthetic spectra or possibly spectral/population components (called ‘feature files’) which cover a wide range of plasma parameters. That is, to optimise the speed of the fit, the feature generation code will be separate from the fitting itself.

5.2.2 Opacity

Provided the plasma does not fall outside the moderate optical depth regime for which the escape factor technique is valid, one can use the continuous escape factor code of chapter 3 to allow optically thick series limit spectra to be modelled. This produces an escape probability as a function of wavelength that can be used in equation (5.1) as a modification to the escaping flux.

The opacity adjustments to the high lying populations can be done in a number of ways. In the absorption factor approach, the Λ values are used as parametric adjustments on the Einstein A-values in the collisional-radiative matrix. This is straightforward for low lying discrete lines where there is one unique Λ for each transition. For the higher series lines, there is some ambiguity as to whether an emitted photon originated from one upper level or from its neighbour. One approach is to split the high level populations into population elements, with corresponding frequency elements in the evaluation of Λ . The justification for this is that, as the levels merge together, it is no longer meaningful to talk about a discrete population and arbitrary elements of population can be defined. One can then evaluate rate expressions for all these ‘elements’ and insert them into the new collisional-radiative matrix to produce a population structure using Λ s evaluated for each of these frequency elements. For future application to non-Maxwellian distributions this is the appropriate method to adopt.

An alternative approach is to consider discrete level populations, with corresponding rates for each level. One then considers the absorption from the resultant total intensity due to any overlapping profile at the right frequency to be absorbed by that line. That is, our absorption factor expression becomes:

$$\Lambda = 1 - \frac{\int_{\Delta\nu} \alpha_{discrete}(\nu) I_{blended}(\nu) d\nu}{\int_{\Omega} \int_{\Delta\nu} \varepsilon_{discrete}(\nu) d\nu d\Omega} \quad (5.2)$$

where the frequency integration is over the one high series spectral line profile, and the emission and absorption coefficients correspond to the values for that discrete line, i.e. no line blending is accounted for. It is only in the intensity term that the fully blended emission and absorption coefficients are considered.

This approach has the advantage that it requires minimal changes to the existing C-R code framework. Rates already exist for these high n-shells, and the Λ values evaluated here can be included directly. Figure 5.2 shows some results for this technique, generated using the high quantum shell Λ code from chapter 3 - note that, as expected, the absorption factors increase as one progresses up the series. It should be noted that for the 14 – 2 transition and above, the lines are blending together significantly, and at higher optical depths one sees a slight decrease in absorption factor for these transitions. This is due to the fact that the radiation field causing the photo-absorptions is due to all the overlapping profiles and thus is greater than that produced if the emitting line was isolated. This naturally leads to more photo-absorptions in the line under investigation and hence a reduced absorption factor. This effect has been also been noted in the thesis of Fischbacher (2001). As the density increases the absorption factors decrease, as one would expect (recall the definition of the absorption factor in equation (1.14)).

It is easier to deal with the continuum opacity modifications to the population structure. The rates that are used in the collisional-radiative codes are all Maxwell averaged ones, thus it is most appropriate to evaluate an absorption factor that is also averaged over the whole continuum and can be used as parametric adjustments on the spontaneous recombination rates. A procedure has been written to evaluate this (see section 3.4.1), and the results are shown in figure 5.3 for an electron density of $1 \times 10^{14} \text{ cm}^{-3}$ and an electron temperature of 1eV.

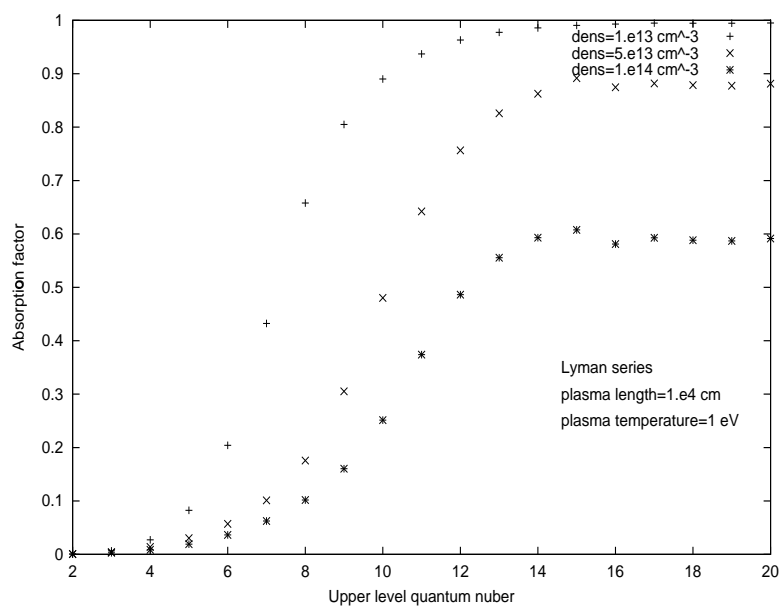


Figure 5.2: Continuum absorption factors as a function of upper level quantum number for the Lyman series for a plasma with $T_e = 1 \times 10^4 K$, $length = 1 \times 10^4 cm$ and a range of plasma densities.

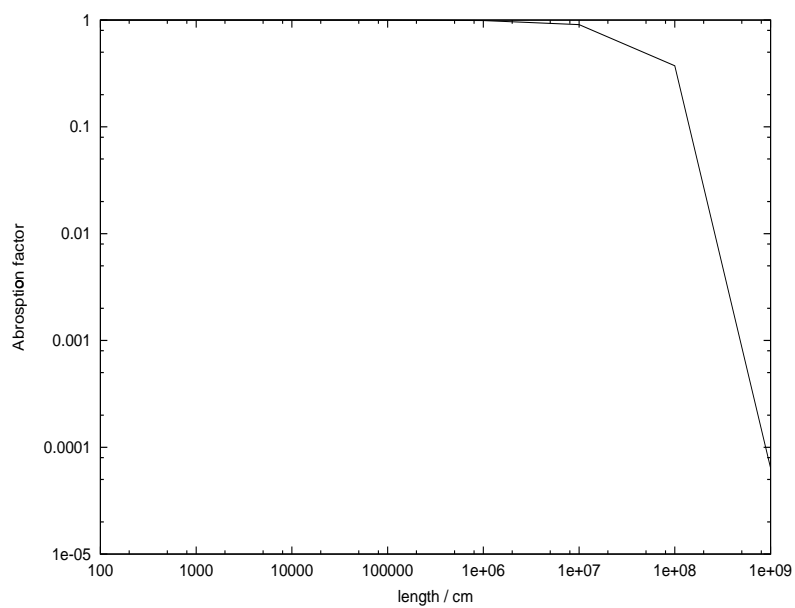


Figure 5.3: Continuum averaged Λ for the Lyman continuum plotted as a function of plasma length with $N_e = 1 \times 10^{14} \text{ cm}^{-3}$, $T_e = 1 \text{ eV}$. Results are generated using the code of chapter 3

5.2.3 Line profile evaluation

Spectral line profiles are evaluated as described in chapter 3. The expression of Griem (1960) is used as the basic profile for all levels, but is substituted as appropriate for key observed lines by improved approximations. Here such high quality profiles are calculated by the PPP code (Talin et al., 1995, Talin et al., 1997). PPP is used for approximately the first fifteen series members. Calculation of the higher series members is somewhat computationally demanding, but is also of less importance, allowing the Griem profiles to be used. These line profile calculations are combined with the population results to evaluate the bound-bound contribution to the emission coefficient.

It is interesting to compare the line profile expressions as evaluated by the Griem equation with those evaluated using the PPP code. The profiles are primarily dependent on the electron density, but also vary with the electron temperature. Figure 5.4 shows the Griem profiles overplotted on the PPP results for a range of densities. It was found that the Griem profiles produce profiles extremely close to the PPP results up to densities of $\sim 2 \times 10^{14} \text{cm}^{-3}$ for typical divertor temperatures ($\approx 1 \text{eV}$). For densities above this, the Griem profiles underestimate the electron broadening and thus produce profiles which are too narrow. Our primary interest for this work is in the divertor region of tokamaks with densities from $(0.1 - 5) \times 10^{14} \text{cm}^{-3}$, thus we are in the regime where the Griem expression is starting to break down. Nevertheless, it will still produce good profiles for many of the densities that one would want to investigate, and for densities beyond its region of validity the PPP profiles are used.

5.2.4 Bound-free, bremsstrahlung and impurity contributions

The higher bound-free hydrogen continuum contributions are evaluated from expressions such as equation (3.6). In the spectral feature code, a routine first developed for analysis of the bremsstrahlung emission in the JET tokamak (Horton, 2001) formed the basis for evaluation of all the hydrogenic bound-free contributions. The Horton procedures agreed exactly with an independent routine developed here. For compatibility with ADAS and other applications, it was decided to base the work here on

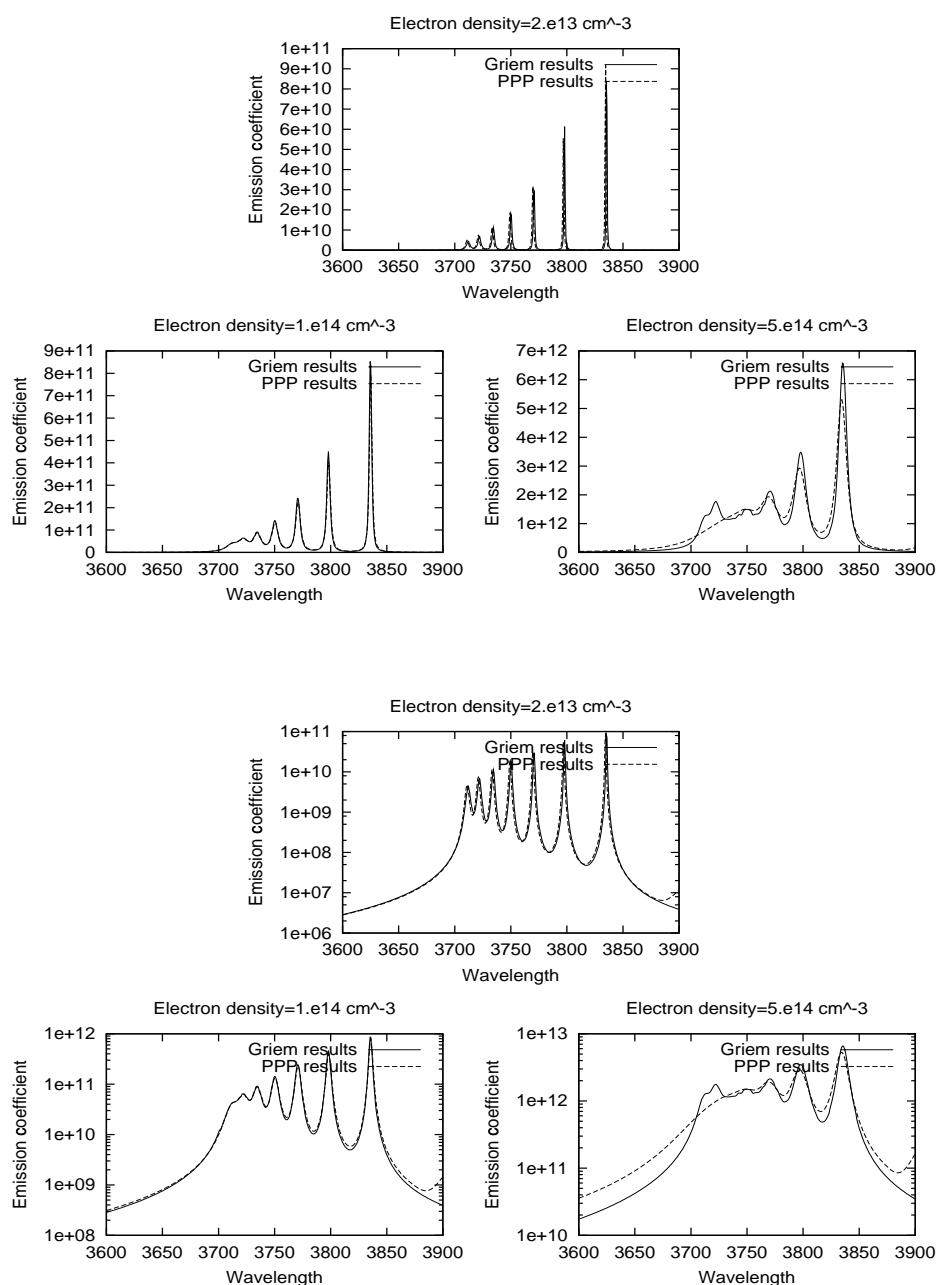


Figure 5.4: The resultant bound-bound emission coefficient evaluated using the collisionally broadened profiles of Griem (1960) compared with those from the PPP line broadening code. The lower set of plots show the results on a logarithmic y-axis. The first fifteen profiles of the Balmer series are evaluated. Note that the discrepancy at large densities is largely due to the Lorentzian profiles not being good extensions from Griem's profiles for these plasma parameters.

the Horton procedures. The hydrogen bremsstrahlung contribution from the Horton code is evaluated from analytic hydrogenic expressions given by Burgess & Summers (1987). Horton's code also evaluate all the continua from impurity species. For this it requires information on the ionisation and recombination coefficients for each ionisation stage of the impurity in question. This information is obtained using the ADAS subroutine d2data.for which in turn accesses atomic data from ADAS adf11 files. Note that all ionisation stages of an impurity are included

All the continua contributions from all possible impurity species are generated within the spectral feature calculation by this method. The impurity emitters may originate from a different region of the line of sight than the hydrogen emitters. Thus the code allows for different temperatures, densities and length of emitting regions in the impurity calculation.

5.3 A specific code for modelling the Balmer emission in the JET divertor.

5.3.1 Details of the physical problem

With the possibility of generating a complete spectral feature incorporating the continuum edge, a much more complete comparison with spectral observations is now possible. The main study here is as a potential diagnosis tool for the JET divertor. A description of divertor conditions and typical high series spectra has been given in chapter 1. In this region, one sees a strong Balmer series limit spectrum when the plasma detaches from the divertor wall. Under these circumstances it is no longer possible to rely on langmuir probe temperature and density measurements (such probes are embedded in the divertor walls) and alternative pure spectroscopic techniques such as this high series one become of value. The plasma parameters in this case are extracted by fitting a synthetic spectrum to the complete series limit and continuum edge observations. This has in fact been done with some success by Pigarov et al. (1998). See section 3.3 for a description of the differences between the approach presented here and the one used by Pigarov. The plasma parameters which

can be deduced in principle are the electron temperature from the free-bound continuum slope and intensity ratio of the high series members, the electron density from the width of the high series lines, the recombination state from the series decrement and, if the impurity contribution to the emission is significant, the Z-effective and impurity concentrations from the underlying continuum level.

The JET KT3 spectrometer was used to measure the high series Balmer spectra. KT3's line of sight 'sees' about 70% of the outer divertor target as shown in figure 5.5. It is estimated from the JET plasma transport codes that the Balmer emission originates from approximately 2-3 cm of the divertor region for the vertical plate discharge and 3-4 cm for the horizontal plate discharge, though these values have large uncertainties. As one can see from figure 5.5 the line of sight of KT3 passes through the centre of the tokamak cross section so the total observed intensity will potentially contain contributions from outwith the divertor region. In the experiment the KT3 instrument takes a sequence of temporal shots over a single JET pulse. Information is generated from each track (i.e. spatial position) at each time slice. KT3 has a spatial resolution of 13mm and 0.1nm spectral resolution. An exposure time of 100 msec was used for the high-n Balmer observations. Note that the spectrometer is able to measure the Paschen continuum edge and the spectral feature code is also able to model this spectral region. An analysis of Paschen spectra has yet to be performed. From Meigs et al. (1998) typical JET divertor conditions would be an electron density of $\sim 1 \times 10^{14} \text{ cm}^{-3}$, neutral deuterium density of $\sim 1 \times 10^{13} \text{ cm}^{-3}$ and electron and ion temperatures of $\sim 1 \times 10^4 \text{ K}$.

5.3.2 Modelling work

Population results

Figure 5.6 shows the b-value results of the population code for an electron density of $1 \times 10^{14} \text{ cm}^{-3}$, and electron temperature of $1 \times 10^4 \text{ K}$. It can be seen that the atomic populations reach Saha-Boltzmann values by about $n = 5$. The b-values in figure 5.6 correspond to the datafile shown in figure 5.1. Examination of the datafile shows that the excited level populations are largely populated through recombination (i.e.

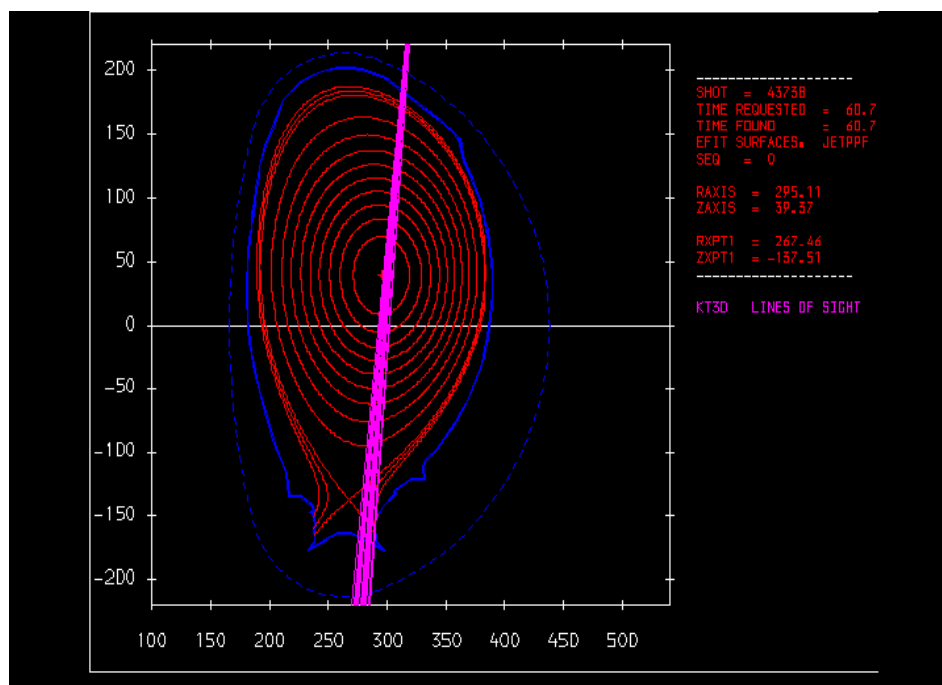


Figure 5.5: Illustration of the lines of sight of the KT3 instrument in the Balmer series limit observations.

the contributions to b_n come largely from the F2 column), as one would expect from a strongly recombining plasma.

Thus, for the higher Balmer series transitions which are of interest here, the upper level populations are close to their thermodynamic equilibrium values. Also, one can have confidence that the free electrons will have a Maxwellian velocity distribution, making the hydrogenic continua expressions for Θ and ε (which assume Maxwellian distributions) valid. Despite the fact that TE values would be sufficient, the spectral feature code takes the evaluated b-values into account to allow for extension to NLTE conditions if necessary.

Opacity results

The opacity code of chapter 3 was run for the selected divertor conditions and as expected the plasma is optically thin both from an emergent flux and a population point of view for the spectral region (see figure 5.7). Thus Θ can be set to one for the

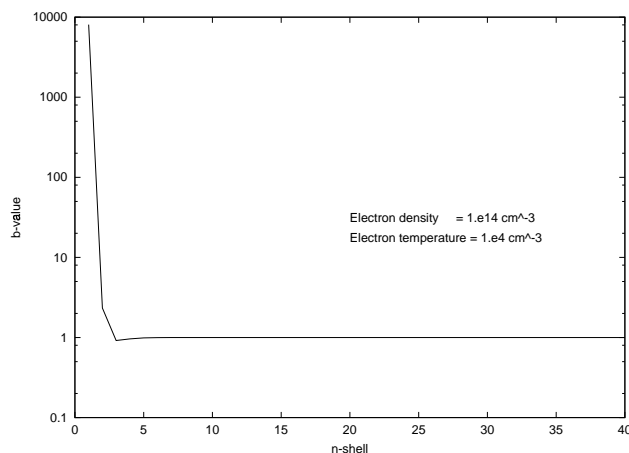


Figure 5.6: Population b-factors vs principal quantum shell for divertor conditions.

emergent flux calculation and no population adjustments are necessary for the higher series transitions.

As has already been shown in figure 1.11, the lower Lyman lines are likely to be optically thick. An optically thick population calculation was performed to evaluate the effect of Lyman series photo-absorption on the excited state population structure. ADAS 214 was used to generate the optically thick adf04 for population processing via ADAS 205, see figure 5.8. It can be seen that the $n=2, 3$ & 4 shells all have enhanced populations. Upon closer investigation it was found (for an electron density of $1 \times 10^{14} \text{ cm}^{-3}$) that the increase in the $n=2$ population is due to photo-absorption, while the increase in the $n=3$ & 4 populations is mainly due to electron excitation from the enhanced $n=2$ shell, with the effect becoming less pronounced as one increases in n -shell. Thus there is an indirect influence of opacity on the populations for $n > 3$. As was seen from figure 5.1, recombination dominates over collisional excitation for the highly excited states, and these opacity effects are not likely to change this. However, the photo-absorption enhanced population of the $n=2$ shell and subsequent collisionally enhanced populations of the higher shells must be included for completeness in the final ADAS code to allow lower series members to be modelled correctly. Thus for the series limit work presented in this chapter opacity is considered to have a negligible effect on the highly excited populations.

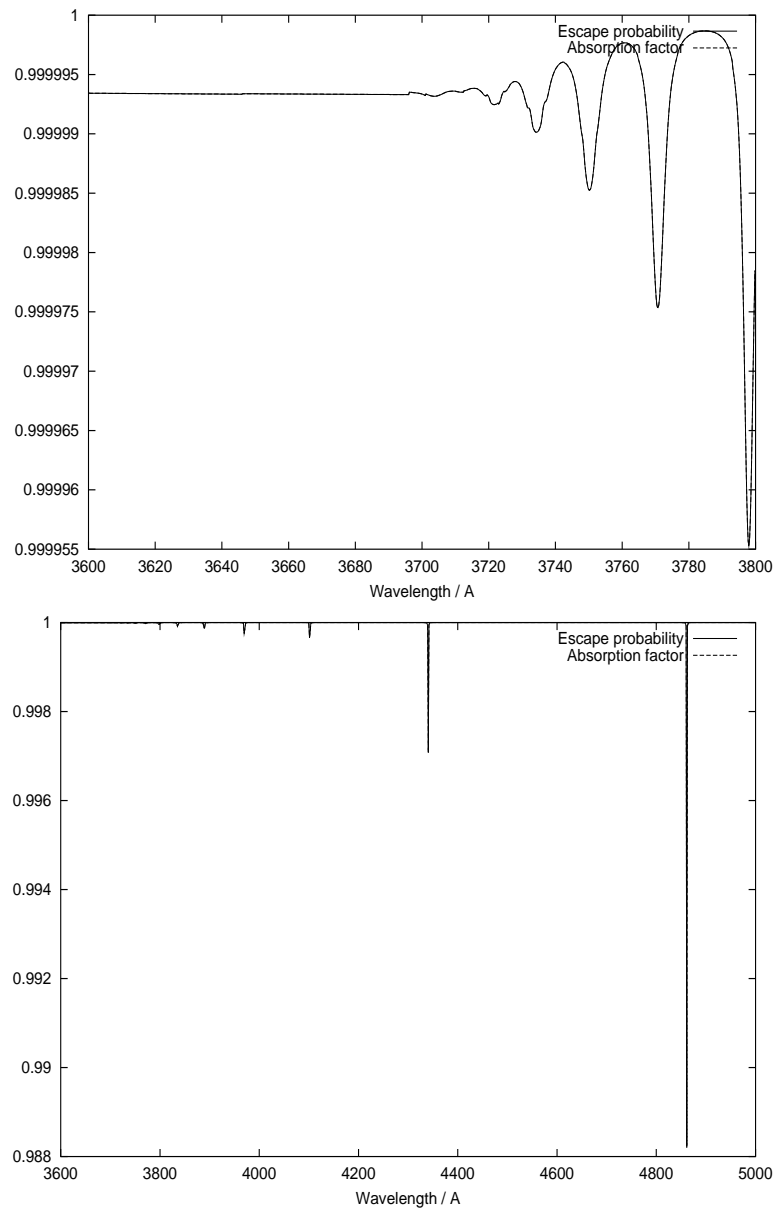


Figure 5.7: Analytically continuous escape probabilities and absorption factors vs. wavelength evaluated for typical divertor conditions. The upper plot shows the results near the series limit and the lower plot the results including lower series members. Note that on both scales, the factors are negligible.

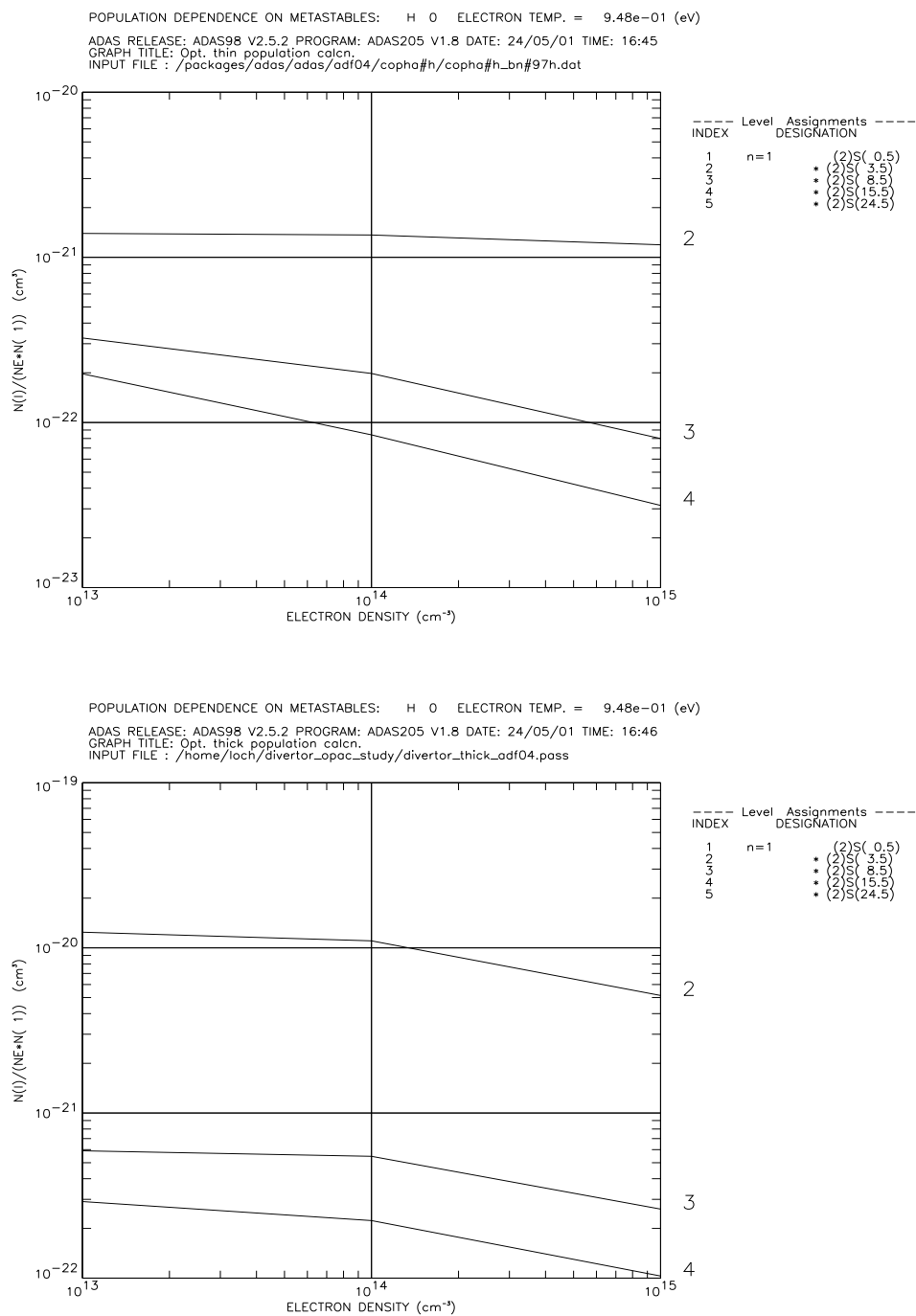


Figure 5.8: Upper plot shows the optically thin excited population densities for the first five n-shells for typical divertor conditions. The lower plot shows the optically thick results.

Hydrogen bound-bound, bound-free, bremsstrahlung results and impurity contributions

The emission coefficient as evaluated in the code is made up of many components. Figure 5.9 shows the hydrogen bound-bound, bound-free and bremsstrahlung contributions for the case of an electron density of $1 \times 10^{14} \text{cm}^{-3}$, electron temperature of 1eV and a line-of-sight length of 10cm . Note that the other hydrogen continua, in particular the Paschen continuum makes a significant contribution to the resultant spectrum at the minima between discrete series lines. The bremsstrahlung contribution is the least significant, but must still be accounted for.

In order to evaluate the impurity contributions to the emission it is necessary to know the impurity concentrations in the divertor plasma. Typical values for JET are given in McCracken et al. (1998). Figure 5.10 shows the contributions to the total intensity of the synthetic spectrum from carbon, oxygen and beryllium impurities at the median concentrations of McCracken (i.e. impurity concentrations of 1 %, 1 % and 0.2 % of the deuterium density respectively). The impurity contribution, although present, does not significantly alter the synthetic spectrum. For the results shown in figure 5.9 and 5.10 the hydrogen b-b, b-f and impurity emitters were given identical line of sight lengths, electron densities and temperatures.

Note that the inclusion of the various continuum contributions (even at the 10 % level) significantly alters the diagnostic values returned by a fit to the observed spectrum. If these contributions are excluded then a higher electron density is inferred - the fit procedure increases the model density to broaden the lines so that the minima between discrete lines can be matched.

5.3.3 Fitting the JET data and diagnostic results.

Fits were performed on data from two different density runs where the tokamak was configured such that the strike point was on the vertical and then on the horizontal plates of the divertor (JET pulse numbers 43735 and 43738). Observational data from KT3 was available for these two pulses for a range of time slices and track numbers. For consistency it was decided to examine the results from track number 6 for both

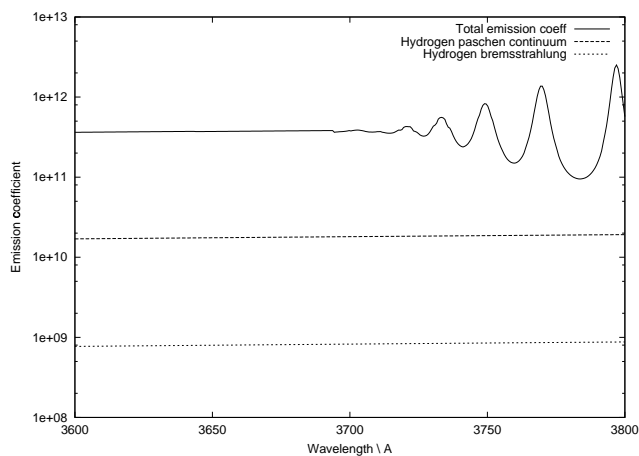


Figure 5.9: Contributions to the emission coefficient from the different hydrogen components. The code was run for $N_e = 1 \times 10^{14} \text{ cm}^{-3}$, $T_e = 1 \text{ eV}$, emitting length = 5.5 cm . The bremsstrahlung emission is assumed to come from the same emitting region as the bound-bound and bound-free components.

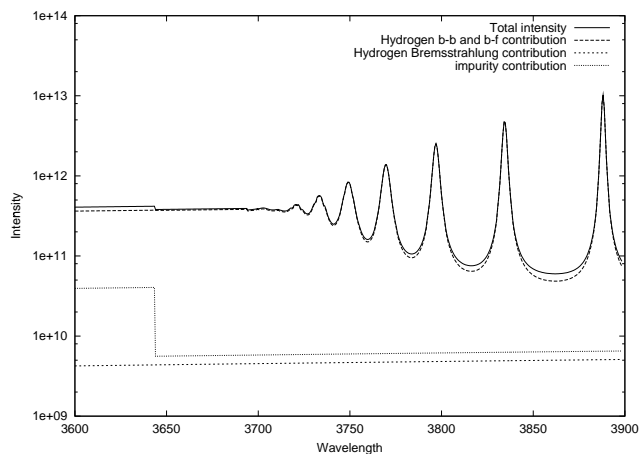


Figure 5.10: Contributions to the total intensity from all the hydrogen and impurity emitters. The input parameters were as in figure 5.9. The step in the impurity contribution is because the impurity code assumes hydrogenic continuum edges for each ionisation stage.

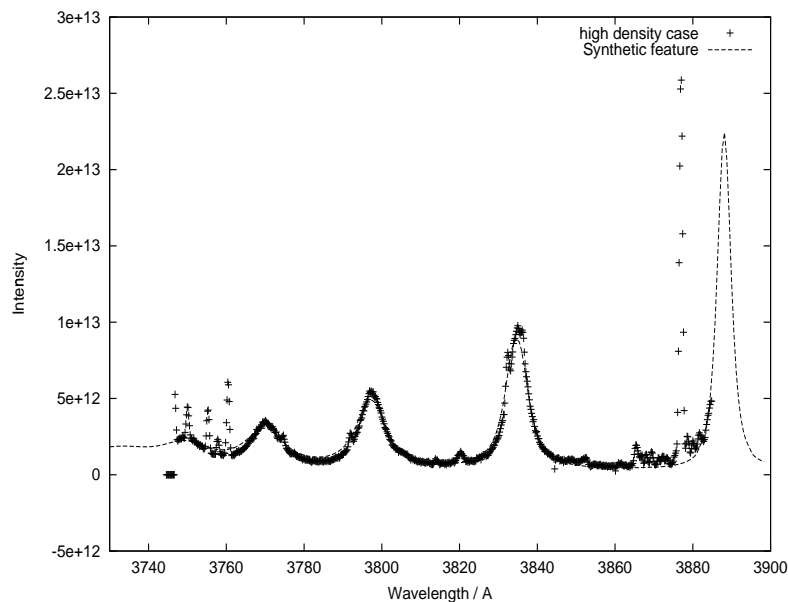


Figure 5.11: Diagnostic fit to pulse 43735, Balmer series limit spectrum, track 6, $t=18.95s$

pulses. An analysis of these pulses has already been performed (Meigs et al., 1998 and Meigs et al., 2000) where the FWHM of the 9-2, 10-2 and 11-2 lines were measured and the electron density inferred. An electron density is deduced by Meigs for each of the three lines independently using a Stark profile expression from Breger, 1998. For a meaningful comparison to be given, it was decided to model each pulse at a time slice for which FWHM data and hence diagnosed electron density had been obtained. Figure 5.11 shows our optimised fit to the data of pulse 43735. Note that the fit was optimised iteratively by hand. The automatic least squares optimising of the feature to the data is in development as a future ADAS code. The diagnostic values from the fit are shown in table 5.1 with the results from the FWHM analysis of Meigs shown in table 5.2.

The second fit performed was to the results of pulse 43738. Figure 5.12 shows our fit to this lower density data. The deduced parameters are shown in table 5.3 and the FWHM results in table 5.4.

Physical quantity	Value for synthetic feature
Electron density	$3 \times 10^{14} \text{ cm}^{-3}$
Ion density	$3 \times 10^{14} \text{ cm}^{-3}$
Electron Temperature	1 eV
Length of line of sight	3 cm
Impurities	Carbon, Oxygen, Beryllium
Impurity abundances	1%, 1%, 0.2%

Table 5.1: The diagnostic values returned from the fit shown in figure 5.11

Balmer line	FWHM \AA	Diagnosed density cm^{-3}
9-2	4.6792922	$4.19 \times 10^{14} \text{ cm}^{-3}$
10-2	5.8150216	$4.29 \times 10^{14} \text{ cm}^{-3}$
11-2	7.5598365	$4.29 \times 10^{14} \text{ cm}^{-3}$

Table 5.2: Diagnosed electron densities from the FWHM analysis of Meigs.

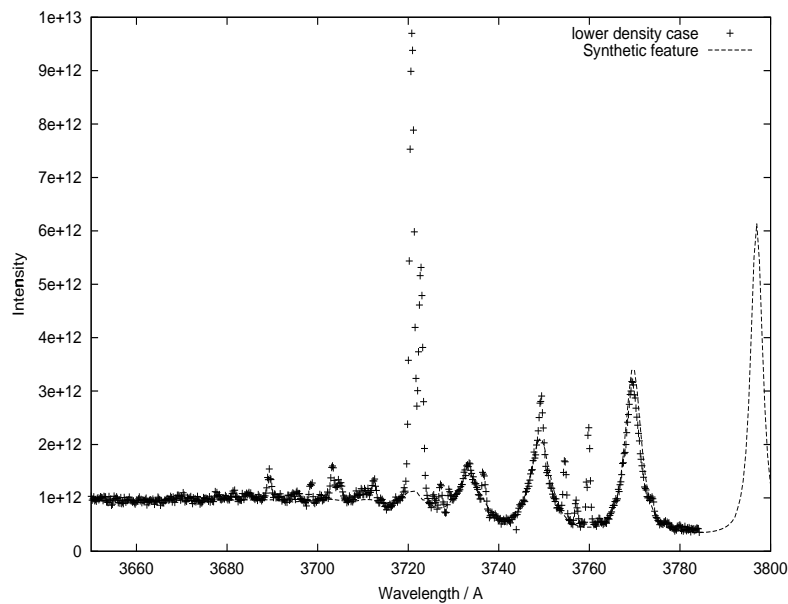


Figure 5.12: Diagnostic fit to pulse 43738, Balmer series limit spectrum, track 6, t=19.45

Physical quantity	Value for synthetic feature
Electron density	$0.85 \times 10^{14} \text{ cm}^{-3}$
Ion density	$0.85 \times 10^{14} \text{ cm}^{-3}$
Electron Temperature	1 eV
Length of line of sight	16 cm
Impurities	Carbon, Oxygen, Beryllium
Impurity abundances	1%, 1%, 0.2%

Table 5.3: The diagnostic values returned from the fit shown in figure 5.12

Balmer line	FWHM \AA	Diagnosed density cm^{-3}
9-2	2.7419637	$1.88 \times 10^{14} \text{ cm}^{-3}$
10-2	3.6132523	$2.10 \times 10^{14} \text{ cm}^{-3}$
11-2	4.5239519	$2.10 \times 10^{14} \text{ cm}^{-3}$

Table 5.4: Diagnosed electron densities from the FWHM analysis of Meigs.

Discussion of the fit

As one can see from the graphs and the optimised input parameters, reasonable fits have been achieved. The present fits to the spectra yield systematically lower densities than those returned from the FWHM analysis. This is because the continuum contributions are not considered in the FWHM analysis. As was indicated in section 5.3.2, neglecting the complete set of continuum contributions can lead to an inferred electron density that is spuriously high. Failure to account for all continuum contributions may also explain a similar discrepancy noted as point (iii) of the series limit analysis of stellar flares in Zarro & Zirin (1985).

It should be noted that obtaining an optimal fit as shown above is not just a matter of matching the line widths on the high series lines. The code returns the absolute intensity of the spectrum and it is necessary for this to match the observations as well. Thus the line widths, degree of line blending and absolute intensity all have to be correct for a good fit to be achieved. This internal consistency adds value to the diagnostic parameters returned from the fit.

Some development of the code is required before it can be used as a diagnostic tool. The first thing to note is that there are many variables that affect the fit. An unconstrained multi-variable optimised fit would certainly reveal many local minima and an ambiguous set of ‘optimised’ parameters. A number of the variables, such as impurity concentrations are only weakly orthogonal from the point of view of continuum emission. The number of search parameters must be reduced, or some ‘global optimisation’ of a whole range of diagnostic measurements including this present series limit one must be adopted. For the demonstration here, we have felt able to specify a number of parameters to a reasonable degree of accuracy independently (especially impurity abundance and length of emitting region) to allow the remaining parameters to be varied and a meaningful fit achieved. We note that the the line-of-sight length used in the fit of pulse 43735 is longer than one might expect. For typical divertor models, the length of emitting region is $\sim 3 - 5\text{cm}$. It is probable that contributions to the measured intensity also came from the part of KT3’s line-of-sight passing through the core of the plasma. A possibly improvement to our method is to use the KS4 instrument as a second reference spectrometer. It is similar to the KT3 instrument, except that its line-of sight excludes the divertor region. This could be used to determine the contribution to the intensity from regions outside the divertor and hence be used to adjust the KT3 observations. Even with this it is probably necessary to model the predicted intensity as originating from two different emitting regions within the divertor as is done in Pigarov et al. (1998). More information from JET plasma modelling codes is needed to guide such an approach.

5.4 Conclusions

The generation of complete series limit spectral features has been demonstrated and the fitting of such features to JET divertor observations shown. Good fits were achieved for both a ‘low’ ($N_e \sim 0.85 \times 10^{14}\text{cm}^{-3}$) and a ‘high’ density ($N_e \sim 3 \times 10^{14}\text{cm}^{-3}$) observation. The next stage will be to tailor the code to be more specific to the JET divertor setup, for example taking into account all of the emission from the line of sight, not just those from the divertor, and diagnosing the impurity content

for the JET pulses that were analysed.

This work is planned for the immediate future, the aim being to have a code that can perform an optimised fit to the JET high series Balmer observations from the divertor region and return diagnostic information on the local plasma electron temperature and electron density. This will be incorporated into the existing JET data analysis software. The proposed code will perform a least squares fit, and will cycle through multiple spectra once the initial fitting parameters have been set. In developing this code, advantage will be taken of the structure of the existing ADAS fitting routines.